REVIEW ARTICLE
https://doi.org/10.1038/s41560-022-01096-5

nature energy

Advances and challenges in understanding the microscopic structure–property–performance relationship in perovskite solar cells

Yuanyuan Zhou[1,2] ✉, Laura M. Herz[3,4], Alex K-Y. Jen[5,6] and Michael Saliba[7,8]

The emergence of perovskite photovoltaic technology is transforming the landscape of solar energy. Its rapid development has been driven by the advances in our understanding of the thin-film microstructures of metal halide perovskites and their intriguing correlations with optoelectronic properties, device efficiency and long-term stability. Here we discuss the morphological characteristics of three key microstructure types encountered in perovskites, which include grain boundaries, intragrain defects and surfaces. To reveal detailed structural information of these microstructure types via tailored characterizations is crucial to probe their detrimental, neutral or beneficial effects on optoelectronic properties. We further elaborate the impacts of these microstructures on the degradation modes of perovskites. Representative examples are also presented, which have translated fundamental understandings to achieve state-of-the-art perovskite solar cells. Finally, we call for more attention in probing hidden microstructures and developing high-spatiotemporal-resolution characterizations, as well as harnessing the potential merits of microstructural imperfections, towards an elevated understanding of microstructure–property–performance relationships for the next solar cell advances.

The need for decarbonizing our current energy generation has driven an intense search for novel photovoltaic technologies that can deliver high power conversion efficiencies (PCEs) at a low manufacturing cost. In 2009, Miyasaka and co-workers[1] reported a type of photovoltaics that used metal halide perovskites (MHPs) as light absorbers. The subsequent use of MHPs in engineered thin-film device structures triggered excitement, which led to the advances in perovskite solar cells (PSCs) to produce PCEs to a certified 25.7% with excellent stability parameters that approach industrial standards[2–13]. A typical PSC consists of a centre layer of MHP sandwiched by an electron-transport layer (ETL) and hole-transport layer (HTL) (Fig. 1a)[14]. MHPs generally adopt the ABX_3 structure (Fig. 1b), in which A is a monovalent cation, such as methylammonium (MA^+), formamidinium (FA^+) or Cs^+, B is Pb^{2+} or Sn^{2+} and X is I^-, Br^- or Cl^-. The family of MHPs now extend to embrace lower-dimensional members with tailored crystallographic structures[15], which offer intriguing optoelectronic properties and stabilities. This unlocks a wide material range to optimize single-junction, tandem and multijunction PSCs in addition to opening novel fundamental questions.

For any given MHP, the microstructure is the most critical factor that determines the properties and thus device performance[16]. For PSCs, the most straightforward performance parameters are the PCE and stability. PCE is a product of the open-circuit voltage (V_{OC}), short-circuit current density (J_{SC}) and fill factor measured under one-sun illumination. All three parameters are affected by photocarrier transport and recombination processes in the MHPs, and they are intimately related to the film microstructure[17]. Regarding the PSC stability, the key challenge is the relatively low materials stability of MHPs under external stimuli, such as heat, moisture, oxygen and electric fields[17], which is related to the microscopic transport of intrinsic and extrinsic ionic and/or molecular species in MHP films. In addition, the (opto)mechanical reliability of perovskite, which is microstructure dependent, can influence the PSC stability[18]. Therefore, it is unsurprising that the technological advances in PSCs were largely driven by an improved understanding and rational engineering of the MHP microstructure and associated morphological defects, as illustrated in Fig. in Box 1 (see Box 1 for a discussion of the figure details)[16,17,19]. In fact, MHPs exhibit an unconventionally variable microstructure, regarded as both a blessing and a curse: although the extremely facile processability of MHPs opens the door to a wide, yet precise, control over the microstructural features, the soft nature of MHPs renders their deterministic characterizations challenging[15,16]. The coexistence of opportunities and challenges stimulated intense research aimed to elucidate the intriguing structure–property correlation to reveal the mechanistic origins of PSC efficiency and stability losses[15,20,21].

This review groups performance-limiting microstructural features into three types on the basis of where morphological defects extend in MHP films: grain boundaries (GBs)[17,22–26], intragrain defects (IGDs)[19,26–28] and surfaces[11,29–33]. By examining updated findings from recent representative studies related to these three microstructure types, we create a unique knowledge hub that connects four key aspects of previous perovskite research works: characterization techniques, structural variations, properties and device performance. Meanwhile, we provide insights into these findings that not only evoke classical materials theories, but also expand the territories of materials and energy sciences. Specifically, first, we review recent advances in morphological characterizations of the three MHP microstructure types. The unique capabilities of

[1]Department of Physics, Hong Kong Baptist University, Hong Kong, China. [2]Smart Society Lab, Hong Kong Baptist University, Hong Kong, China. [3]Clarendon Laboratory, Department of Physics, University of Oxford, Oxford, UK. [4]TUM Institute for Advanced Study, TU Munich, Garching bei München, Germany. [5]Department of Chemistry, City University of Hong Kong, Hong Kong, China. [6]Hong Kong Institute for Clean Energy, City University of Hong Kong, Hong Kong, China. [7]Institute for Photovoltaics, University of Stuttgart, Stuttgart, Germany. [8]Helmholtz Young Investigator Group FRONTRUNNER, IEK5-Photovoltaik, Forschungszentrum Jülich, Jülich, Germany. ✉e-mail: yyzhou@hkbu.edu.hk

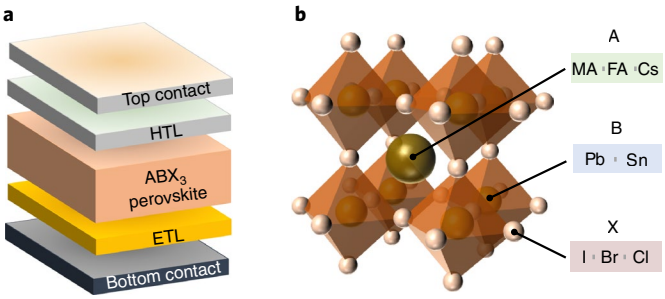

Fig. 1 | Description and progress of PSCs. a, Schematics showing the layer-by-layer device structure of a typical PSC. **b**, Schematic structure of the MHP semiconductor family (chemical formula, ABX_3) most typically implemented in PSCs.

various powerful microscopic characterization tools are leveraged to yield reliable, complete imaging of these microstructure types. Then, we discuss the effects of these microstructure types on the photophysical properties of MHPs, followed by an elaboration of their impacts on the degradation modes of MHPs, with examples of state-of-the-art PSCs achieved via translating such fundamental understandings. Finally, we present perspectives on the emerging directions to address the missing, yet critical, information on the microscopic structure–property–performance relationships of MHPs for further technological advances in PSCs.

Morphological characteristics of MHP microstructures

Microstructure is defined as the structural or chemical inhomogeneities that are formed by spatially distributed components that differ from the perfect crystal lattice[34]. In modern materials science, with the advance in microscopy, microstructure encompasses the length scales of micrometres down to (sub)nanometres. Numerous characterization efforts are invested to unravel the microstructural details of MHPs, which feature a range of unique characteristics that distinguish MHPs from conventional semiconductors[16,17,19,35].

Grain boundaries. The MHPs in state-of-the-art PSCs possess a polycrystalline microstructure with crystal grains of microscale sizes. GBs are the most studied microstructural feature so far, not only because of their prominent existence and confirmed effects on properties, but also owing to the relative ease in identification and characterization as compared with those of IGDs and surfaces[16,36]. Usually, MHP GBs are identified based on the grooving morphologies developed during film processing[37]. The GB characteristics proved to influence the PSC behaviour are density and groove angle on the film surface. GB density corresponds to the average grain size, which can be qualitatively examined using scanning electron microscopy (SEM; Fig. 2a–c). It statistically reflects the extent to which light and charge carriers may be scattered in an MHP film. It is generally revealed that a reduction in GB density, concluded from SEM observations, can generate an overall positive effect on the PSC performance. Regarding the GB groove angle, it is measurable based on the surface topography profile acquired using atomic force microscopy (AFM; Fig. 2d–f). GB grooves potentially leads to imperfect contacts between the MHP and other layers and also to trap solvents and moisture, which impacts the physical and chemical properties at the film surface and/or interface. Nevertheless, SEM and AFM only provide the basic morphological characteristics of GBs, whereas more quantifiable characteristics, which include the degree of disorder, number of coincidence site lattices (sigma values), crystallographic directions of the GB tilt and/or twist classification, specification of GB planes and exact chemical compositions, have to be resolved by knowing the relevant atomic information. Transmission electron microscopy (TEM) of MHPs was therefore explored with limited success[38]. This is primarily due to the relatively high beam sensitivity of MHPs, which not only prevents reliable TEM observations with a normal electron dose but also challenges the acquisition of focused-ion-beam (FIB)-based sample specimens. Although the field is still in the process of exploring optimal specimen preparation and imaging methods, by leveraging low-dose scanning TEM (STEM), atomic-scale structural information of perovskite microstructures was imaged in directly deposited and FIB-based MHP film sample specimens (Fig. 2g–i), which offer plan and cross-section views, respectively[19,39]. In particular, Rothmann et al.[19] showed that in a thermally evaporated $FAPbI_3$ MHP thin film, although many GBs are morphologically sharp with a low degree of disorder, some GBs are highly disordered. Such atomic-scale structural variations between different GBs suggest one possible origin of the discrepancy on the GB effects on MHP properties[19]. In fact, the variation of the local (dis)order of GBs has been widely studied in other materials systems, but the inclusion of A-site organic cations differs in MHPs, and how the organic–inorganic complexation affects the local (dis) order of GBs remains unknown, pointing to a fascinating area in fundamental materials research.

Although tailored TEM characterization provides both plan and cross-section views of GB structures in MHP films, the GB network in practical PSCs can be even more complex to assess. The MHP layers in state-of-the-art PSCs are as thick as about 1 µm, as compared to the 10-nm-thick thin films studied by Rothmann et al.[19] In such films, GBs can be frequently buried (Fig. 2j), which prevents regular surface-based observations and so calls for tomographic techniques. In this context, a new tomographic AFM method was developed, which entailed a high load applied to the conductive AFM tip to probe and instantaneously polish the film surface to expose the buried bulk features[40]. By acquiring numerous 2D maps at increasing film depths, 3D film tomography is then constructed to present a view of the 3D GB network as reflected by the photoconductivity contrast. As seen in Fig. 2k, buried GBs can present a different distribution from that of the top view and usually the GB density in the near-bottom region is higher. This can be a critical finding, as the bottom side is where the light illuminates during PSC operation and these buried GBs may exhibit more influence than bare GBs on the optical, electronic and chemical properties of MHPs. This concept of tomographic imaging may be extended to TEM[41], which can potentially yield 3D images with atomic detail.

Another important geometric parameter of GBs is the misorientation angle, which describes the relative orientation of two crystal grains with respect to each other by either tilting or twisting (Fig. 2l). Misorientation can reflect the structural coherence of two crystalline planes, and therefore it will affect the atomic-scale interaction of GBs with electronic carriers, ions and molecules in MHPs. Although Kelvin-probe force microscopy (KPFM)[42] is a feasible method to qualitatively differentiate low-angle and high-angle GBs based on the surface potential contrast, electron back-scattering diffraction (EBSD) is the workhorse for the accurate quantification of GB misorientations over thin films. In fact, the EBSD characterization of perovskites was not considered successfully until the recent use of a low-dose, high-sensitivity detector[43]. Figure 2m shows a typical inverse pole-figure map of a $MAPbI_3$ MHP film acquired using EBSD. Jariwala et al.[43] showed that a higher spread in misorientation within MHP films leads to more severe non-radiative carrier recombination, mostly related to the increase in local strain heterogeneity.

Intragrain defects. IGDs have started to draw attention in the field, as it is frequently observed that reducing GBs does not necessarily result in PSC performance enhancement[39]. The relatively frequent existence of IGDs in MHPs is attributed to the softness of the crystal

Box 1 | Evolution of the perovskite microstructure along the technological progression of solar cells

The figure displays a roadmap showing the evolution of MHP film and device microstructures in record PCE PSCs over time. Sketches in the regions (1)–(8) illustrate the essential PSC structures (omitting HTLs and top contacts) from cross-section views. SEM images in the regions (1)–(11) show top-view microstructures of the MHP films in the corresponding devices, except that in (3) is viewed with slight tilting. The SEM image in region (7) is also a top view (the inset shows the cross-section). The roadmap reveals three characteristic development periods for the PSC technology. This first period (2009–2014) demonstrates the effort to improve the absorber films of $MAPbI_3$ MHPs to a smooth, compact and polycrystalline microstructure, which led to the steepest increase of PCEs from 3.8 to 16.1%. The second period (2014–2015) mainly features a composition transition of MHPs ($MAPbI_3$ to $FAPbI_3$) to extend the light absorption while maintaining the compact polycrystalline film microstructure. In the latest period (2015 to date), the effort was devoted to nanoscale or even atomic-scale modifications of GBs, IGDs and surface/interface microstructures in the $FAPbI_3$-based MHP thin films. Specifically, region (1) shows the first version of a PSC with a $MAPbI_3$ MHP fabricated in a discontinuous, quantum-dot morphology and deposited on a mesoporous TiO_2 ETL[1]. Here, the yellow circles and white arrow in the SEM image point to the MHP quantum dots loaded on TiO_2. Region (2) illustrates a later version in which the perovskite forms a continuous nanoscale thin layer on mesoporous TiO_2 ETL[2]. Region (3) shows a PSC in which $MAPbI_3$ MHP fills the mesoporous TiO_2 ETL and forms a pillared capping layer[3], and the uniformity of such capping $MAPbI_3$ MHP layers was then improved by the adoption of so-called sequential deposition, which leads to a PSC structure, as shown in region (4)[4]. In region (5), solvent engineering is invented for the $MAPbI_3$ MHP fabrication to create a compact, polycrystalline film morphology[5]. The subsequent studies were devoted to achieve a near-pure $FAPbI_3$ composition to extend the light absorption while creating compact films with a reduced GB density, and successively led to the device structures shown in regions (5)–(7)[6,7]. This record was then topped with a protocol that enabled the manipulation of the internal iodine vacancies in $FAPbI_3$ thin films, as seen in region (8)[8]. In more recent years, PCE advances were led by the passivation of the $FAPbI_3$ MHP top surface using different two-dimensional (2D) phases, as shown in regions (9) and (10)[9,10], and the simultaneous passivation of both the top surface and GBs using a pseudohalide additive[11], as shown in region (11). Here, the cross-sectional SEM image of the pseudohalide-engineered MHP film is shown in the inset of the top-view SEM image. A certified 25.5% PCE was achieved via the atomic-scale engineering of coherent interfaces between the buried $FAPbI_3$ MHP surface with the SnO_2 ETL, as shown in region (12)[12]. An optimal PSC may be created in the

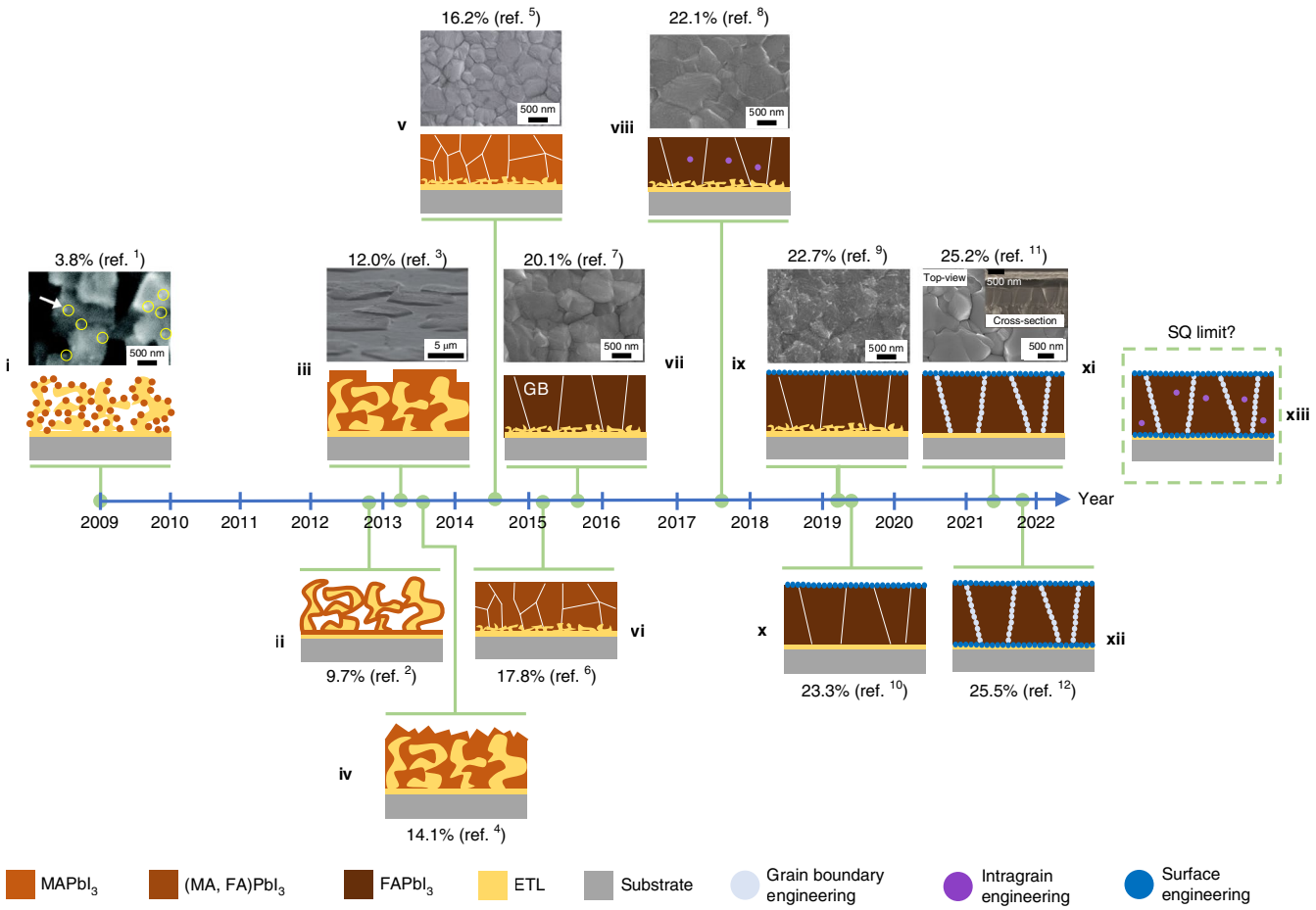

Box 1 | Evolution of the perovskite microstructure along the technological progression of solar cells (Continued)

future that simultaneously optimizes GBs, IGDs and surfaces, which may lead to stable PCEs that approach the Shockley–Queisser (SQ) limit, as shown in region (13). The evolution of detailed PSC structures reflects the urgency in tailoring GB, IGD and surface microstructures in a more targeted and precise manner, because such enhanced microstructures can potentially mitigate detrimental effects, as well as harness any potential merits, on the electronic transport and ionic and/or phase stability of MHPs and PSCs. SEM images adapted with permission from: **i**, ref. [1], American Chemical Society; **iii**, ref. [3], Springer Nature Limited; **v**, ref. [5], Springer Nature Limited; **vii**, ref. [7], AAAS; **viii**, ref. [8], AAAS; **ix**, ref. [9], Springer Nature Limited; **xi**, ref. [11], Springer Nature Limited.

lattice, which allows high tolerance to local disorder within crystalline grains. Although considered electrically active, IGDs are rarely visible under regular SEM or AFM, for which their effects have been omitted. Nevertheless, the advances in the TEM of MHPs facilitated the confirmation of a range of IGD types[19,44,45], which include coherent twinning boundaries (CTBs), stacking faults (SFs), dislocations and point defects (Fig. 3a-e)[19].

CTBs refer to the special boundaries formed between high symmetry lattices (Fig. 3f). One possible formation mechanism of CTBs in MHPs is based on the facile polymorphic transformation that occurs in the grain interior during film processing or on device operation. For instance, the $MAPbI_3$ perovskite can exhibit a cubic-to-tetragonal phase transition near 50 °C when cooled from a typical processing temperature of over 100 °C. The twin domains formed can extend across the whole crystal grain with a few hundred nanometre width. It was revealed that they reversibly (dis) appear across the tetragonal-to-cubic phase transition temperature, which attests the proposed formation mechanism[44]. In addition, the crystallographic structure of these twins is usually found to be consistent with the classic 90° *a*–*a* domains that are formed in barium titanate perovskite via similar phase-transition processes[44,46].

SFs refer to those planar defects in which the proper order of stacking planes is interrupted, and two unconventional types of SFs have been identified in MHPs. The first is the Ruddlesden–Popper (RP) fault, which is chemically expressed as $(AX)(ABX_3)_n$ ($n=\infty$) and usually observed in inorganic MHP nanocrystals-assembled films[45]. One intriguing structural feature of RP faults is that they can extensively propagate within MHP grains and frequently form right-angle steps. This creates unusual intragrain interfaces with added structural dimensionality. The tolerance to such kinked SFs may be attributed to a high internal strain in nanoscale MHP domains. The other type of MHP SFs are structurally formed by a partial shift of adjacent crystal planes, which exhibit a limited dimension of a few tens of nanometres and cannot form kinks (Fig. 3g)[19,39]. The formation of these SFs is mostly related to MHP synthetic conditions, as there is evidence that shows their density is tailorable via post-treatment[47]. The morphological difference between the two SF types could lead to different effects on photocarrier transport and stability.

Dislocations (1D) and point defects (0D) are lower-dimensional defects that can be intrinsically formed in MHPs or easily created during the device operation. Compared with GBs, CTBs and SFs, the lower dimensionality of these defects may cause relatively localized effects on properties. In particular, dislocations may form channels of higher conductance in MHP films, which can be harnessed to tailor film carrier mobilities[48]. Also, dislocations and point defects are relatively mobile. On external stimuli, such as an electrical field, light, strain and thermal conditions, they can interact with 2D crystallographic defects, such as GBs, CTBs and SFs to form charge-carrier traps and add to the complexity in degradation modes[39]. In general, characterizations of dislocations and point defects in MHPs are even more challenging due to the structural dimension encountered and strict sample geometry required[19,38]. Although the atomic morphologies of edge dislocations (Fig. 3h) and vacancies (Fig. 3i) of certain types have already been experimentally confirmed in the MHP films ($FAPbI_3$) (ref. [19]), screw dislocations and interstitial ions have not been imaged yet, which leaves a vast space for future discoveries.

Unlike the case of GBs, reports on MHP IGD tailoring are rare, whereas a recent study by Li et al. has proved its feasibility via both composition and processing engineering; Fig. 3j shows TEM images of $MA_{1-x}FA_xPbI_3$ MHPs with x varying from 0 to 1 (ref. [47]). In $MAPbI_3$, $\{112\}_t$ (t, tetragonal) CTBs (determined using electron diffraction) were observed in almost all grains, which are reduced to only half when 10 mol% FA is incorporated. When x is further increased, all the $\{112\}_t$ CTBs basically disappear and a different type of CTB or SF starts to emerge with $\{111\}_c$ (c, cubic) boundaries. Furthermore, Li et al.[47] showed that the preparation methods influence the formation of IGDs. Solution-processed $MA_{1-x}FA_xPbI_3$ ($x \geq 0.5$) MHPs can show a much higher density of $\{111\}_c$ IGDs than that of a thermally evaporated $FAPbI_3$ MHP film. Post-treatment of MHPs using MA–thiocyanate vapour annealing can also change

Fig. 2 | Morphological characteristics of MHP GBs. a–c, GB characterization using SEM: schematics of the SEM method (**a**), schematics of GB density characteristics measurable using SEM (**b**) and a typical SEM image (top view) of an $FAPbI_3$ MHP film (**c**). **d–f**, GB characterization using AFM: schematics of the AFM method (**d**), schematics (cross-section) of GB groove-angle characteristics determinable using AFM (**e**) and a typical AFM topographic image of an $FAPbI_3$ MHP film (**f**). **g–i**, GB characterization using SEM: schematics of the STEM method (**g**), schematics of atomic-scale GB characteristics (plan view) measurable using STEM (inset: zoomed-in display illustrating the atomic structure of a GB) (**h**) and a typical STEM image of an $FAPbI_3$ MHP film (**i**). **j**,**k**, Buried GBs in MHPs: schematic illustration (**j**) and segmented cross-sectional tomograms of GBs (top) and grain interiors (bottom) (**k**), which reveal GBs visible at and buried underneath the film surface, respectively. The images were acquired based on the tomographic (conductive) AFM characterization. Blue dash and white dash circles denote the visible and buried GBs, respectively. The colour bar shows the scale of current under this AFM measurement. Sidewall in the top and bottom panels refers to the grain interior and GB, respectively. **l**,**m**, GB misorentation: schematics showing two types of GB misorientation (the blue and green colours represent grains with different orientations) (**l**) and a demonstration of GB misorentation measurements using correlated SEM (left top) and EBSD (inverse pole figure map; left bottom) for an $MAPbI_3$ MHP thin film (**m**). The colour bar in **m** is the index map for the crystal planes of the film surface. The 001 in the IPF colour key indicates that the IPF map plotted is along the sample *z* direction. The black arrows in the SEM and EBSD images show a typical transition of grain orientation across four grains (donated as 1, 2, 3 and 4) and three GBs. The right panel of **m** depicts changes in the local crystal orientation along the black arrow as viewed normal to the sample. H/LAADF, high/low-angle annular dark-field. Panels reproduced with permission from: **c**,**f**, ref. [22], American Chemical Society; **i**, ref. [19], AAAS; **k**, ref. [40] under a Creative Commons license CC BY 4.0. **m**, ref. [43], Elsevier.

the $\{111\}_c$ IGD density. By combining continuous tailoring, density qualification and type determination of various IGDs, a systematic investigation of the intriguing IGD effects on various MHP properties and PSC device parameters is demonstrated, and features an overall negative role for the as-mentioned IGD types in this study (Fig. 3k,l).

Surfaces. The top and bottom surfaces of MHP films (Fig. 4a) interact directly with other device layers and the environment. Thus, they exhibit a strikingly enhanced role on properties due to the nanoscale film dimension as compared with those in bulk materials, in which GB and IGD microstructures dominate. Therefore, surface is discussed as another prominent MHP microstructure type in PSCs[49,50]. In particular, MHP surfaces accommodate intriguing microstructural dynamics that involve the interplay between photophysics and chemistry, as they are formed on continuous interactions of the MHPs with the external environment during processing and later determine the interactions between the MHP layer and the ETL

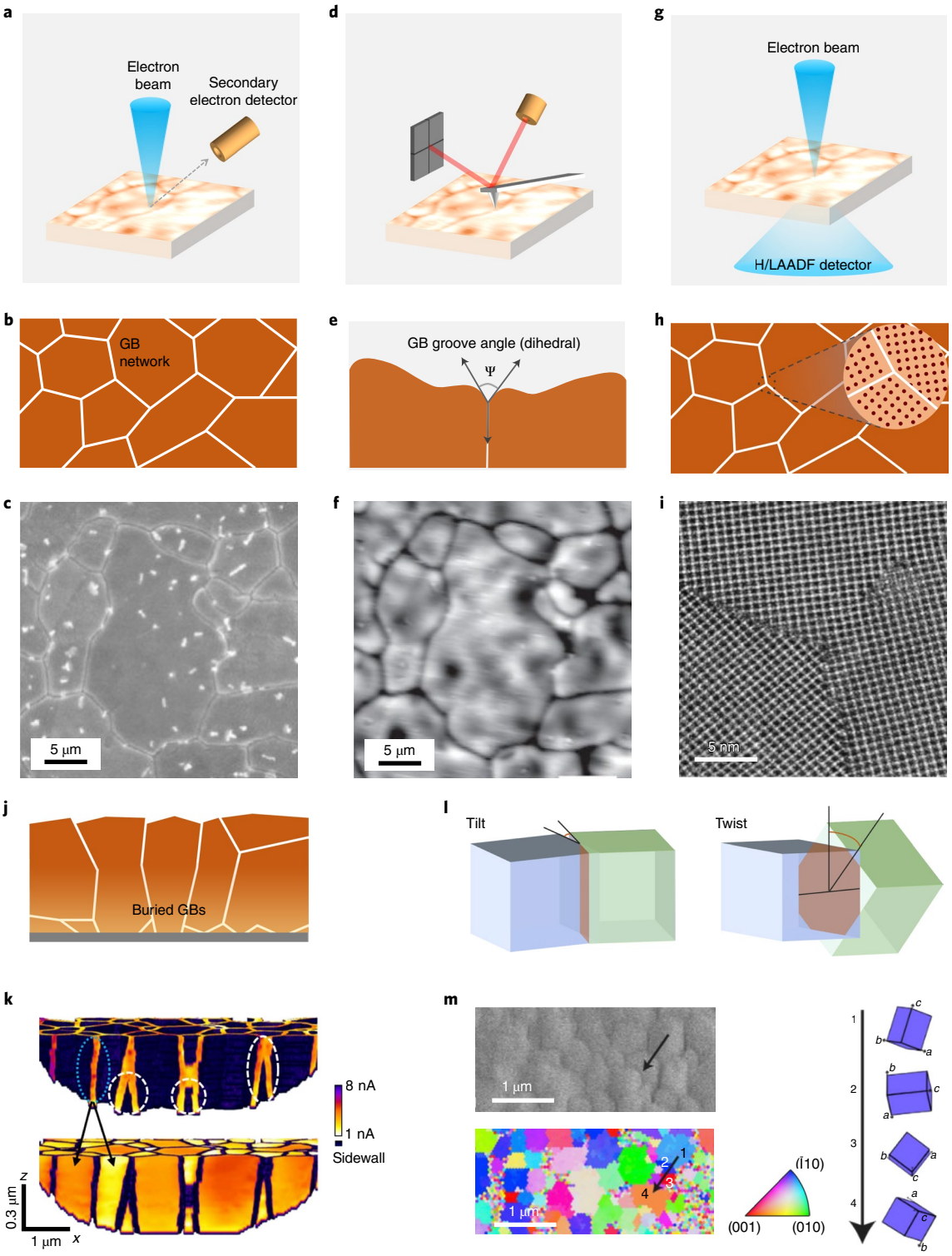

and/or HTL. In this context, the structural characteristics of MHP surfaces will be determined by two aspects, one concerning intrinsic characteristics and the other concerning interface structures when they form junctions with other device layers. Both will potentially influence the transfer of photocarriers with critical impacts on device J_{SC} and V_{OC}[33]. MHP surfaces are also a stability-limiting factor as they favour ionic interactions and movement[51,52].

The intrinsic characteristics of MHP surfaces feature crystallographic facets, chemical terminations and surface point defects. To determine the crystallographic facet of the MHP grain surface is necessary because the properties and structure within any given grain are not fully isotropic. It is unambiguous that statistical manipulation of the orientations of MHP grains can yield improved properties—microscopic studies to elucidate the role of local surface facets await further advances in the EBSD qualification of MHP films. Chemical terminations (Fig. 4b) are extensively studied theoretically, but the experimental determination of chemical terminations in MHPs was not established until the recent advances in solid-state NMR characterization of MHPs[53,54]. This is because using this technique, the binding sites and modes of ligands at the surface become accessible. Surface terminations in MHPs are known to be sensitive to the synthetic conditions[55]. Yuan et al.[56] showed that the use of a dimethylsulfoxide solvent atmosphere can convert PbI_2 termination into AX termination in MHPs via Lewis acid-base interaction, and thereby transform the surface electronic landscape (Fig. 4e). With regard to surface point defects (Fig. 4c), they are visible under scanning tunnelling microscopy[57], and they exist prominently in MHPs mostly for two reasons: (1) the relatively soft ionic bonds in MHPs can create incompletely coordinated sites and (2) surface structures are quantum confined, which allows a higher tolerance to morphological defects. These types of surface point defects can include iodide vacancies, lead antisites and organic-cation vacancies, and create in-gap states and thereby reduce the device voltage. One generic method to engineer the surface point defects is to incorporate a molecular passivator layer via solution processing, which actively interacts with defects and makes them benign (Fig. 4d). Successful passivators reported so far include organic molecules, inorganic salts and organic–inorganic hybrids. As an example, Fig. 4f shows phenethylammonium-passivated $FAPbI_3$, which can enable state-of-the-art PSCs[10]. Furthermore, the chemical termination of MHP surfaces can actually be closely associated with the density of surface defects[29], and thus engineering strategies for chemical termination and surface point defects, as well as crystallographic facets, may be coupled towards the best-performing PSCs.

Heterointerfaces of two types were recently created as novel MHP surface structures to achieve state-of-the-art PSCs, as they can potentially mitigate the issue associated with regular surface treatments, which inevitably introduce a high degree of structural disorder. For type I heterointerfaces, we specifically point to those coherent interfaces formed between MHPs with different dimensionalities (Fig. 4g). Such surface structures can be controllably formed via treatment of the surfaces with solutions that contain bulky or lengthy organic cations, followed by a post-treatment (Fig. 4i) that induces the formation of 2D RP or Dion–Jacobson MHP layers. The dimensionality of the 2D MHP fragments was found to be essential to optimize the passivation effects on both electron- and hole-selective interfaces, which can be controlled either via the post-treatment conditions or incorporated organic cations. Azmi et al.[58] showed that all 2D perovskite passivation layers prepared through thermal annealing mostly create the $n=1$ phase, whereas the formation of $n\geq 2$ phases became more pronounced when room-temperature post-treatment is performed (Fig. 4j). Chen et al.[59] showed that bulkier organic cations lead to 2D MHP surfaces. These studies by Azmi et al. and Chen et al. enabled highly efficient and stable PSCs in normal and inverted architectures, respectively. Type II heterointerfaces are fabricated via an epitaxial growth of a coherent heterolayer on top of the MHPs (Fig. 4h), which significantly enhances the interface integrity and stability. This can be attributed to the introduction of an interfacial strain that suppresses defect migration, and is thus beneficial to device performance. Such heterointerfaces can be achieved by the reaction between the MHP precursor and preburied additives in the as-deposited charge-transport layer (CTL) (Fig. 4i). Min et al.[13] showed a coherent interlayer of $FASnCl_x$ via the chemical reaction between a Cl-containing $FAPbI_3$ MHP film and a Cl-bonded SnO_2 ETL (Fig. 4k), which was found to substantially reduce the photocarrier recombination near the interfacial region while minimally affecting the conduction of extracted electrons. Correspondingly, a certified PCE as high as 25.5% was reported based on this heterointerface.

Local photophysical properties of MHP microstructures

With the capability to reveal the morphological characteristics of MHP GBs, IGDs and surfaces developed, interest turned to unravelling their impact on photocarrier transport at the microscopic scale based on the local profiles of the electronic structures of these microstructural features in the general context.

At GBs, various point defects aggregate and induce self-doping, which causes simultaneous shifts of the conduction band minimum (CBM) and valence band maximum (VBM), that is, energetic band bending. Self-doping to positively or negatively charged GB states induces downward or upward band bending of the CBM and VBM, respectively. Such band bending creates beneficial effects by facilitating the collection of one type of photocarrier, whereas the other type is repelled. In Fig. 5a, the scenario of downward band bending is illustrated, which appears to be the case frequently encountered in MHPs. Nevertheless, CBM lowering can also cause the V_{OC} to drop as the Fermi level tends to shift towards in-gap states. Furthermore, GBs can introduce abundant in-gap trap states, which further accelerate non-radiative recombination. de Quilettes et al.[60] performed correlated PL–SEM characterizations to spatially resolve the PL decay dynamics in $MAPbI_3$ films, which reveal a lower-intensity PL and shorter PL lifetime at GBs compared with those at grain interiors. To further visualize in situ the photocarrier diffusion across GBs, Li et al.[61] developed a wide-field PL distribution method (Fig. 5b) to directly observe carrier diffusion. The results indicate that GBs efficiently block the photocarrier transport (Fig. 5c), which affirms the overall negative role. Nevertheless, the role of GBs in MHPs is still being debated, with some reports conversely showing that GBs could be neutral or even beneficial[40,62,63]. Such discrepancies in the properties of MHP GBs may be related to a real spread in their detailed characteristics and electronic properties, as well as to uncontrolled variations in IGDs and surfaces.

In contrast to GBs, IGDs lead to obviously different influence on the energetics of MHPs. CTBs, owing to their highly symmetric

Fig. 3 | Morphological characteristics of MHP IGDs. a–e, Schematics showing various types of IGDs that exist in MHP single grains: overall proliferation of IGDs (illustrated using grey dash lines) (**a**), CTB (**b**), SF (**c**), dislocation (**d**) vacancy (**e**). **f–i**, Atomic-resolution STEM images of IGDs: CTB (**f**), SF (**g**); dislocation (**h**) and vacancy (**i**). The labelled or highlighted regions in **f–i** show the presence of CTBs, SFs, edge dislocations and vacancy defects. **j–l**, Composition-dependent IGD distributions: low-magnification TEM images of $MA_{1-x}FA_xPbI_3$ MHPs ($x=0$–1) (**j**) and analysis of the systematic relationship among the MHP composition, IGD characteristics, carrier lifetime and V_{oc} deficit (**k**), PCE and H-index (**l**). E_g, bandgap; q, elementary charge; FS and RS, forward and reverse scans for the J-V measurements, respectively; H-index, hysteresis index. Panels reproduced with permission from: **f**,**g**, ref. [39] under a Creative Commons license CC BY 4.0; **h**,**i**, ref. [19], AAAS; **j–l**, ref. [47], Springer Nature Limited.

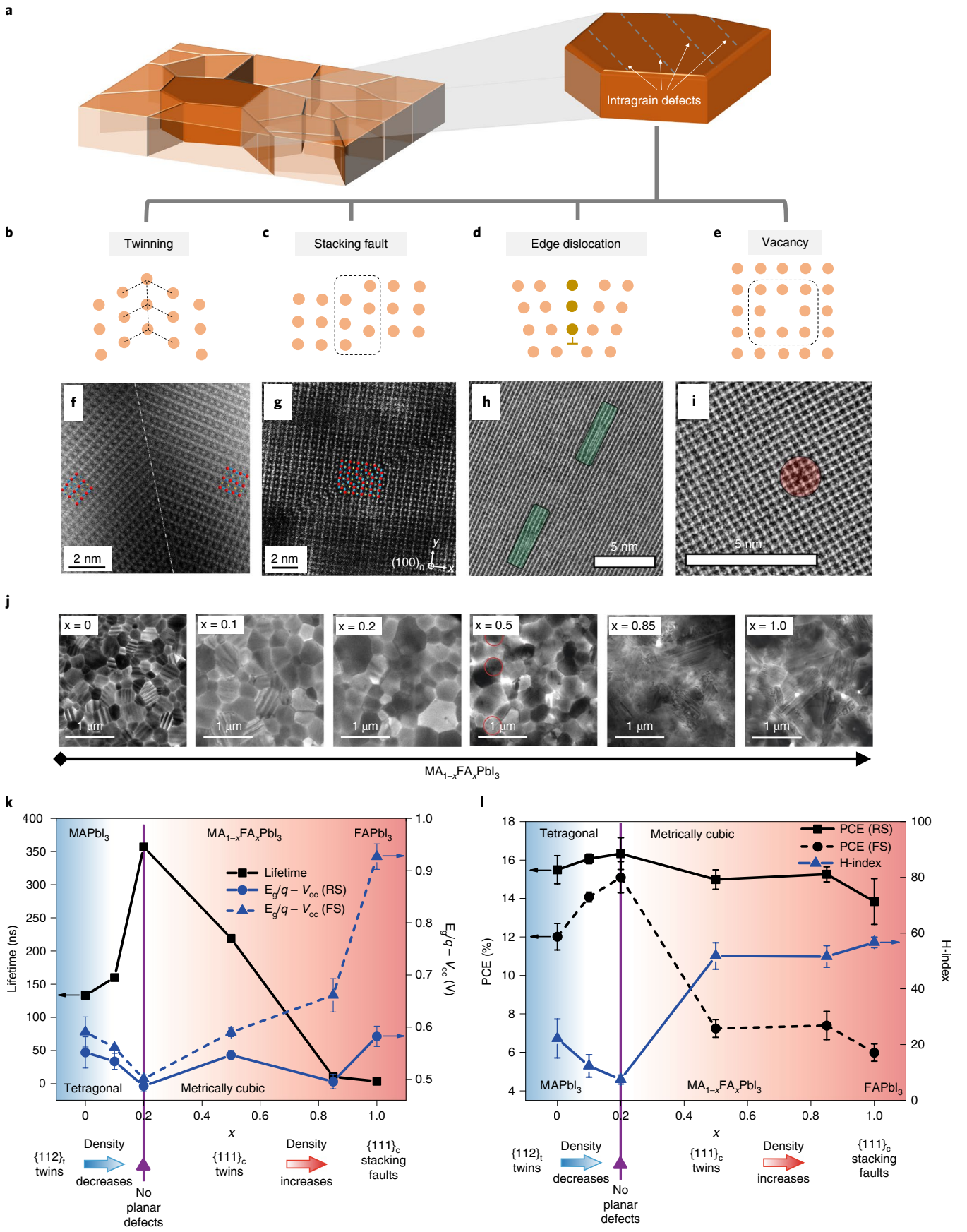
a
Intragrain defects
b
Twinning
c
Stacking fault
d
Edge dislocation
e
Vacancy
f
2 nm
g
2 nm
(100)o
y
x
h
5 nm
i
5 nm
j
x = 0
x = 0.1
x = 0.2
x = 0.5
x = 0.85
x = 1.0
1 μm
MA1−xFAxPbI3
k
MAPbI3
MA1−xFAxPbI3
FAPbI3
Lifetime
Eg/q − Voc (RS)
Eg/q − Voc (FS)
Lifetime (ns)
Eg/q − Voc (V)
Tetragonal
Metrically cubic
x
{112}t twins
Density decreases
No planar defects
{111}c twins
Density increases
{111}c stacking faults
l
Tetragonal
Metrically cubic
PCE (RS)
PCE (FS)
H-index
PCE (%)
MAPbI3
MA1−xFAxPbI3
FAPbI3
x
{112}t twins
Density decreases
No planar defects
{111}c twins
Density increases
{111}c stacking faults

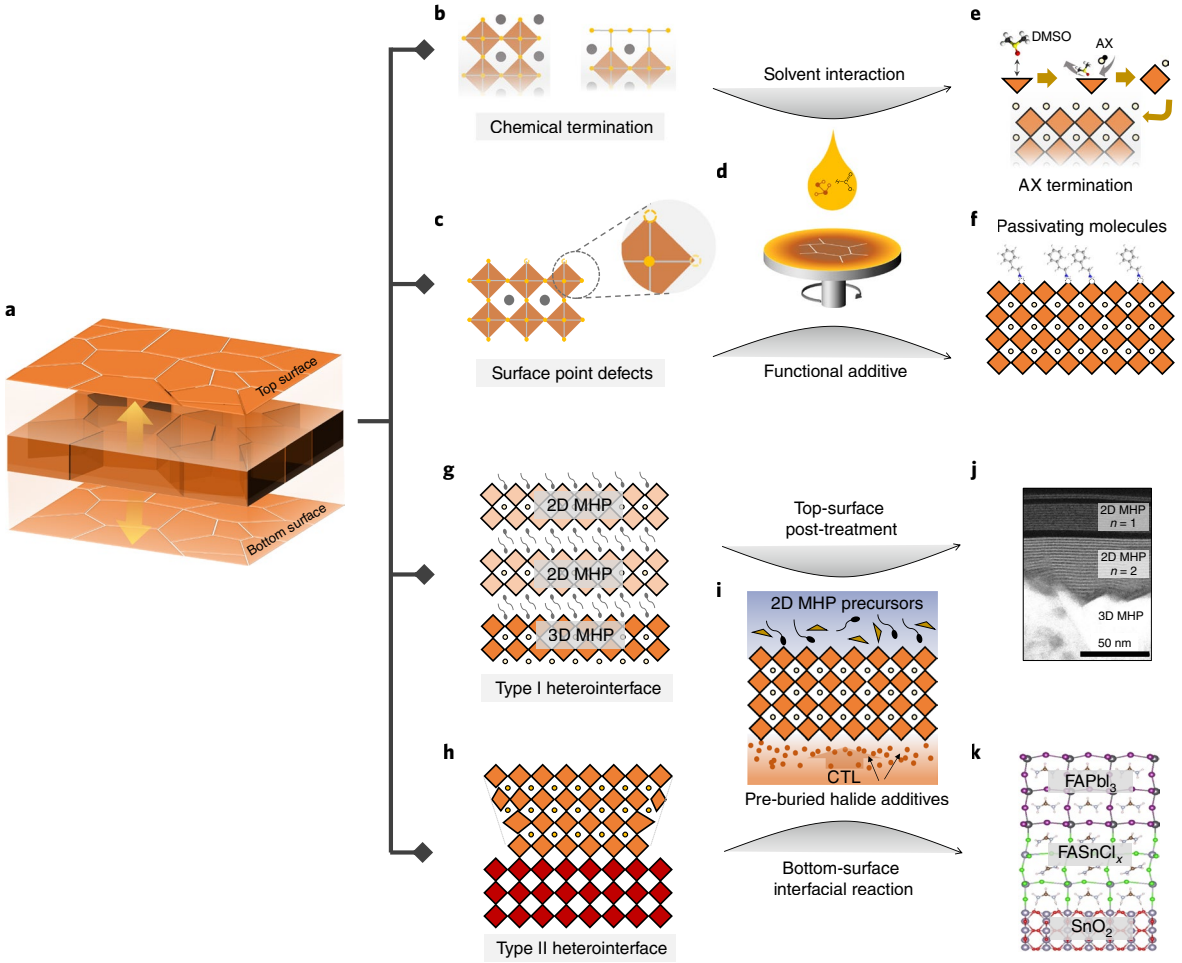

Fig. 4 | Morphological characteristics of MHP surfaces. a, Schematic illustration of MHP surfaces in an MHP film. **b**–**f**, Illustrations of intrinsic surface characteristics. **b**, Chemical termination. **c**, Surface point defects (inset: sketch illustrates an example of halide vacancies on a perovskite octahedral). **d**, Generic method to tailor chemical termination and surface point defects via solution chemistry control. **e**, Representative example using solvent chemistry to tailor chemical termination (AX is the halide precursor for forming an ABX_3 perovskite) and **f** representative example using phenylethylammonium iodide (PEAI) additive to passivate surface point defects. **g**–**k**, Illustrations of the heterointerface characteristics. **g**, Type I heterointerface formed between a 3D MHP and a lattice-matched 2D MHP. **h**, Type II heterointerface formed between 3D MHPs of different compositions (illustrated in orange and red colours) with lattice-mismatch-induced interfacial strain. The irregular quadrilaterals represent distorted perovskite octahedra due to the interfacial strain. **i**, Generic method to form type I and type II heterointerfaces via an interfacial reaction induced by preburied additive and surface post-treatment, respectively. **j**, Representative example showing a type I heterointerface of a 3D MHP with a 2D MHP top layer. **k**, Representative example showing the TEM image of a type II heterointerface of $FAPbI_3$/$FASnCl_x$ on a SnO_2 ETL. DMSO, dimethylsulfoxide. Panels reproduced with permission from: **e**, ref. [56], Elsevier; **f**, ref. [10], Springer Nature Limited; **i**, ref. [59], Springer Nature Limited. Panels reproduced with permission from: **j**, ref. [58], AAAS; **k**, ref. [13], Springer Nature Limited.

structure, induce minimal self-doping under static conditions, which imparts negligible effects on the band alignment and photocarrier transport (Fig. 5d). Xiao et al.[28] assembled a set-up for scanning photocurrent microscopy that records a lateral linear profile of local laser-excited photocurrents across a CTB-containing crystal sample (Fig. 5e). The results show linear photocurrent profiles across the two electrodes at all the bias voltages (Fig. 5f), which reflects the neutral role of CTBs on photocarriers. Nevertheless, the atomic structures of CTBs were not fully confirmed using STEM in this study[28], and thus we should revisit such experimentally observed CTB effects. Furthermore, in the case of mixed-halide MHPs, CTBs can become nucleation centres for phase segregation to form I-rich clusters, which serve as a potential well or barrier for the carrier transport depending on the bulk bandgap[64]. For SFs, the absence of a crystal plane or the shift of a plane can enlarge the atomic distance, which creates a larger bandgap locally, that is, a CBM upward shift and VBM downward shift (Fig. 5g). As a result, a semiconductor–insulator–semiconductor junction will form and repel photocarriers. Thind et al.[45] theoretically studied a RP fault in $CsPbBr_3$ based on a model equivalent (Fig. 5h) to the STEM-revealed atomic structure, which induces no deep defects due to the absence of Pb dangling bonds or Pb–Pb bonds. Figure 5i shows the band diagrams obtained through a layer-by-layer projection of the density of states, and shows band offsets consistent with the CBM and VBM charge density. We hypothesize that the role of RP faults on charge-carrier transport in PSCs may be dependent on their geometrical distribution and its effects on charge percolation pathways to extraction layers. In contrast to the RP fault, other types of SFs are experimentally found to negatively impact the photocarrier lifetime and device parameters, mostly related to the different atomic and bonding arrangement between different types of SFs[47]. Nevertheless, one urgent need is to enable experimentally microscopic observation of individual SFs of each type and their local correlation with (opto) electronic properties. This is challenging as these SFs are rarely

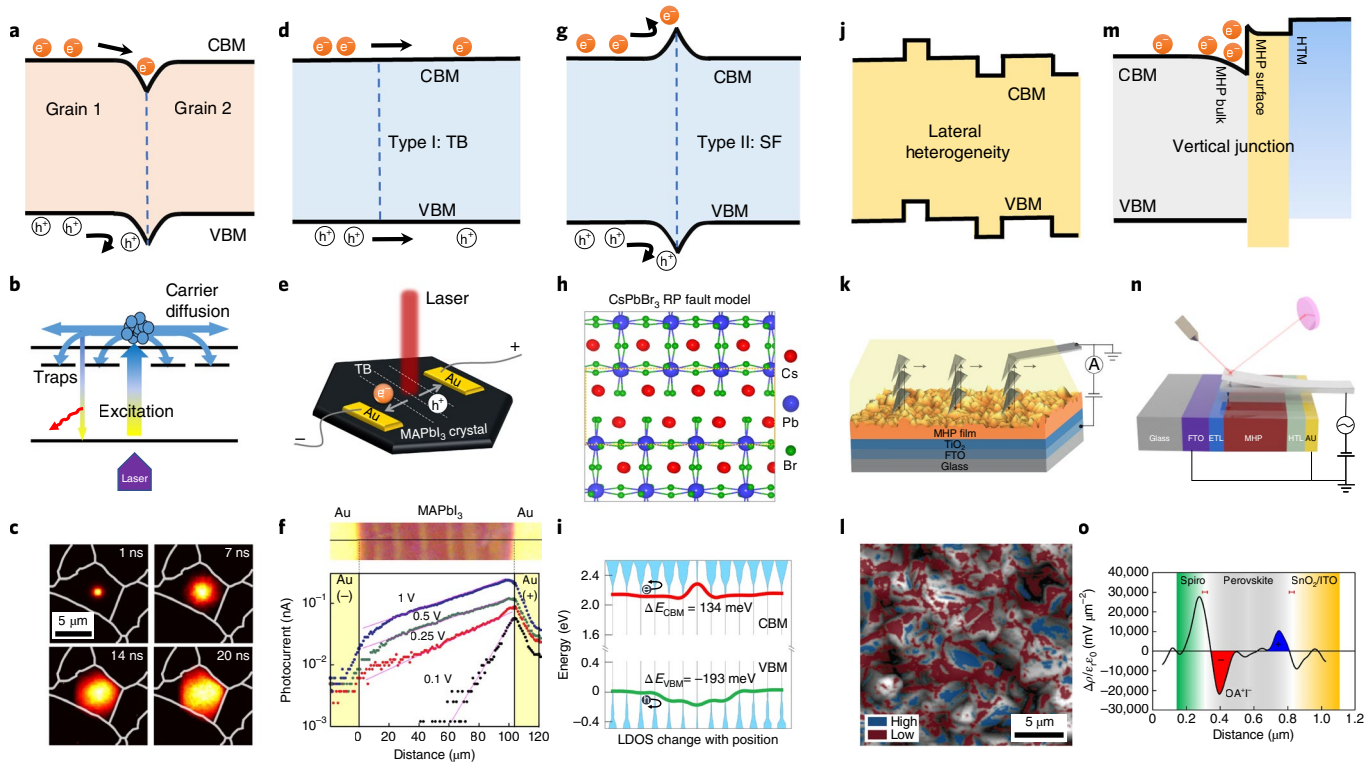

Fig. 5 | Photophysical properties of MHP GBs, IGDs, and surfaces. a–c, GBs: schematic energy diagram at a GB showing a downward band bending (**a**), schematic illustration of a wide-field transient PL imaging method for the in situ visualization of photocarrier diffusion in MHP thin films (**b**) and a real-time image showing the blocking of photocarrier diffusion at GBs observed using the method in **b** (**c**). **d–i**, IGDs: schematic energy diagram at CTBs showing no band bending (**d**); schematic illustration showing the experimental set-up of a scanning photocurrent microscope to determine the carrier transport at CTBs within a GB-free $MAPbI_3$ crystal (**e**), photocurrent profiles (under various electric biases) across the conductive channel within the GB-free $MAPbI_3$ crystal using the set-up in **e** (**f**), schematic energy diagram at a SF showing a downward bending of the VBM and an upward bending of the CBM (**g**), crystal model of a SF equivalent to the atomic-scale structure from a STEM observation (**h**) and layer-by-layer projection of the density of states (LDOS) and bandgap diagram (**i**). **j–o**, Surface: schematic illustration showing the lateral profile of the MHP surface electronic structure (**j**), conductive AFM measurement on an MHP thin film in the PSC device setting (**k**), PCE mapping converted from the J_{SC} and V_{OC} mappings using the set-up in **k** (**l**), schematic illustration showing the vertical profile of the MHP surface electronic structure (**m**), KPFM surface potential mapping based on the FIB-based PSC cross-section to study the vertical energetics of MHP surfaces (**n**) and OAI-treated PSC cross-sections measured by cross-sectional KPFM, which indicates the surface accumulation of electrons (**o**). ρ, charge density; ε_0, vacuum permittivity; ε_r, relative permittivity; Spiro, Spiro-OMeTAD HTL; TB, twinning boundary. Panels adapted with permission from: **e**,**f**, ref. [28], Springer Nature Limited under CC BY 4.0. Panels reproduced with permission from: **b**,**c**, ref. [61], American Chemical Society; **h**,**i**, ref. [45], Wiley; **k**,**l**, ref. [33], Springer Nature Limited. **n**, ref. [92] Springer Nature Limited; **o**, ref. [65], Springer Nature Limited.

visible to other characterizations. We are therefore devoting effort to developing an operando TEM characterization with the integration of an optoelectronic microelectromechanical system chip to visualize the device operation in the presence of IGDs under TEM.

For surfaces, both lateral and vertical energetic profiles are critical to PSCs. Laterally, any heterogeneity in the crystallographic facets, chemical termination and point-defect accumulation leads to heterogeneity in the electrical activities, which can occur at the grain or subgrain scale. In this regard, VBM and CBM profiles on pristine MHP surfaces grown from solution are supposed to form irregular steps with the relative local energy levels influenced by the corresponding structural characteristics (Fig. 5j). Leblebici et al.[33] used a conductive AFM set-up (Fig. 5k) to map the photoelectrical response of grain surfaces, and found spatially correlated heterogeneity in J_{SC} and V_{OC} within individual grains (Fig. 5l). These variations were also linked to crystallographic facets at the nanoscale. Although there is still no systematic investigation to correlate surface termination and point-defect accumulation with properties, theory-guided experimental efforts demonstrated that a uniform tailoring of the surface characteristics can lead to an absolute device improvement, which attests to their important role. Then, assuming that we have achieved a lateral homogeneity in the energy level on an MHP surface via passivation, the vertical energy level alignment across the MHP bulk, surface and ETL and/or HTL (Fig. 5m) becomes another limiting factor, as some passivation could cause a negative work-function change, which drives the formation of a potential well and the accumulation of charges, This drives the halide migration and affects carrier dynamics as well as device stability. Tan et al.[65] showed a modification in the surface treatment method by using octylammonium tosylate instead of the commonly used octylammonium iodide (OAI), and upshifted the vacuum level and minimized the potential well to mitigate the charge accumulation issue, which was confirmed by the KPFM surface potential measurement (Fig. 5n,o).

Degradation modes of microstructures and impact on devices

The most general degradation mode in MHPs is related to the highly volatile nature of organic cations and halide anions, which converts perovskites into PbI_2 or metallic Pb (ref. [66]). This is regardless of compositions. As the movement and removal of these intrinsic ions have to involve breaking of their bonds with the MHP

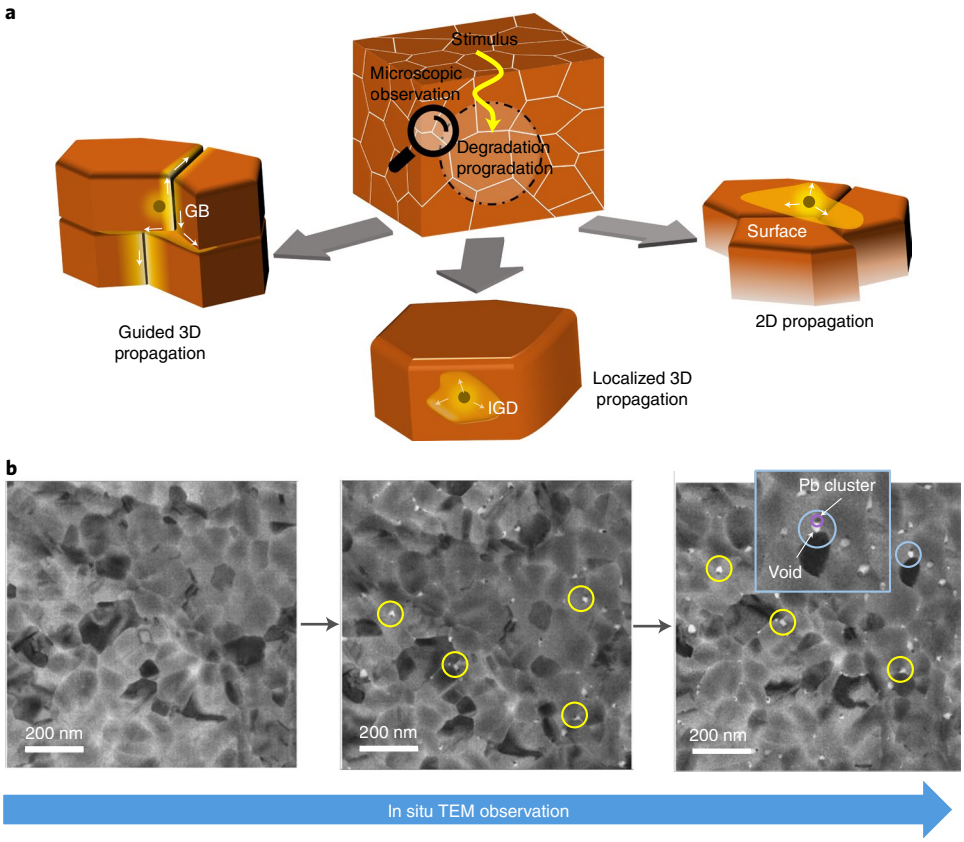

Fig. 6 | Propagation modes of phase degradation processes at different microstructural features of MHPs. a, Schematic illustrations of propagation pathways for degradation that occurs at GBs, IGDs and surfaces. The top figure illustrates the methodology to study the microstructure-dependent degradation dynamics using in situ microscopic observation. The white arrows in the other three figures represent the propagation directions and the dark spots indicate the location at which the degradation initializes. **b**, Example demonstrating an in situ TEM approach to reveal $MAPbI_3$ MHP degradation propagation under electron beam irradiation with Pb clustering at the GBs: the images show the top-view grain and GB microstructures on irradiation at times 4 s (left), 16 s (middle) and 120 s (right). Typical GB regions are highlighted using open circles. Inset: a zoomed-in observation that features the coexistence of a void and a Pb nanocluster. Panel **b** reproduced with permission from ref. [68], Springer Nature Limited under CC BY 4.0.

matrix, it is hypothesized that such degradation will be initialized in those microstructural regions in which more dangling or 'wrong' bonds are accommodated[67]. This was supported by systematic X-ray and optical characterization studies that showed MHPs with an increased population of GBs, IGDs and surfaces[17]. Although the nucleation of degradation in these three types of microstructures can be similar, specific degradation modes vary according to their inherent structural dimensionalities (Fig. 6a).

GBs are interconnected through bulk films to form a 3D complex network. Thus, the decomposition can propagate in relatively facile paths, which leads to a rapid degradation throughout the film bulk. However, IGDs are usually separated from each other in the MHP film. Once degradation occurs, its propagation is expected to be localized. For the surface case, the degradation can occur in a 2D manner, and it can be less constrained compared with that via GBs and IGDs. This implies that different perspectives are needed to engineer GBs, IGDs and surfaces to improve the MHP stability. In situ TEM imaging is desired for the experimental exploration of degradation mechanisms, and has been used tentatively. Alberti et al.[68] acquired a sequence of TEM images of an $MAPbI_3$ film sample in real time (Fig. 6b), and found that metallic Pb clusters initially formed at GBs trigger the perovskite degradation and then migrate preferably along GB network. It is of intrigue that these Pb clusters frequently aggregate at the centres of triple-junction GBs, possibly related to the low energy states offered by the triple-junction geometry. This features the role of GB characteristics on the MHP degradation mechanism. Alberti et al.[68] also found, in some cases, that Pb apparently migrates inside the grains, which can be attributed to the presence of unrevealed IGDs. Although it is also possible that metallic Pb clusters can be formed under an electron beam and vacuum, Alberti et al.[68] carefully excluded these effects by performing control experiments, which is important for in situ TEM studies of MHPs because of their beam sensitivities.

Beyond phase decomposition, a multitude of other composition-dependent mechanisms can affect the MHP stability[69]. We discuss the role of the microstructure on the stability of state-of-the-art MHPs of different types separately: median-bandgap $FAPbI_3$ (ref. [70]), wide-bandgap mixed-halide MHPs[71] and low-bandgap Sn-based MHPs[72,73], which serve as essential units in PSCs from single junctions to tandems. Guided by the revealed mechanisms, we present examples to highlight the importance of microstructural tailoring to the successful implementation in PSCs. We are aware of numerous excellent reviews in the device-oriented research[74–79], and thus we choose to discuss only a few of the most recent representative works.

$FAPbI_3$ suffers from a facile polymorphic transition from the semiconducting α phase to the photoinactive δ phase in the ambient environment, which adds to the difficulty in maintaining its structural stability. This detrimental transition is accelerated in the presence of environmental factors such as moisture[80,81]. In this case, GBs and surfaces are expected to dominate, as they not only offer paths for the interaction and ingression of moisture into the film bulk, but

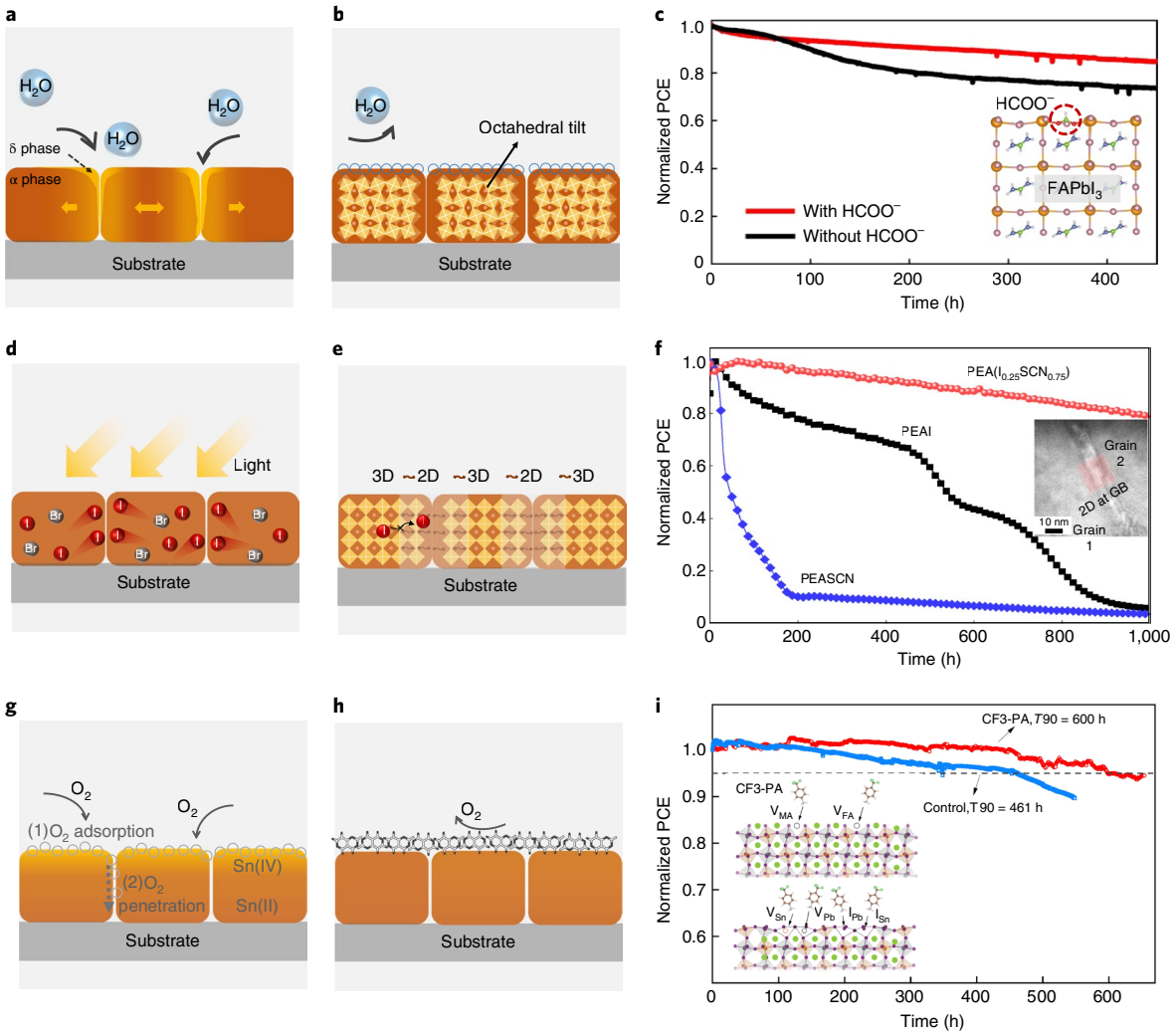

Fig. 7 | Composition-dependent degradation modes of MHPs and impacts on state-of-the-art PSC development. a–c, $FAPbI_3$ MHPs: schematic illustration showing moisture-induced degradation of an $FAPbI_3$ film based on phase transformation, featuring the moisture trapping at GBs and correspondingly accelerated propagation of the α → δ phase transformation (**a**), schematic illustration showing a generic method to stabilize $FAPbI_3$ MHPs, which entails GB and surface functionalization that either repel moisture or tilt the octahedral in the lattice (**b**) and operational stability of a state-of-the-art $FAPbI_3$ PSC made via pseudohalide passivation as compared with that of a normal device (**c**). Inset: schematic illustrating the anchoring of $HCOO^-$ pseudohalide anions on the $FAPbI_3$ surface lattice. **d–f**, Mixed-halide MHPs: schematic illustration showing photoinduced degradation based on halide segregation, which features the iodine aggregation at GBs (**d**), schematic illustration showing a generic method to stabilize mixed-halide MHPs that entails constructing low-dimensional GBs to retard the halide segregation (**e**) and operational stabilities of wide-bandgap $FA_{0.65}MA_{0.2}Cs_{0.15}PbI_{2.4}Br_{0.6}$ PSCs fabricated by GB engineering with a tailored $PEA(I_{0.25}SCN_{0.75})$ 2D phase, pure PEAI and phenethylammonium thiocyanate (PEASCN) (**f**). Inset: cross-sectional TEM of the PSC with GB engineering using 2D phases. **g–i**, Sn-based MHPs: schematic illustration showing oxygen-induced degradation based on Sn(II)-to-Sn(IV) oxidation, which features the first step of oxygen adsorption on the surface and the sequential step of oxygen penetration via the GB network (**g**), schematic illustration showing a generic method to stabilize Sn-based MHPs that entails the stable adsorption of oxygen-resisting, multifunctional molecules (**h**) and operational stabilities of perovskite–perovskite tandem devices with and without CF3-PA passivation (**i**). V_{FA}, FA vacancy; V_{MA}, MA vacancy; V_{Sn}, Sn vacancy; V_{Pb}, Pb vacancy; I, substituted at Sn site (ISn); I, substituted at Pb site (IPb). Inset: multilevel interaction of CF3-PA via the particular Sn defects in Sn-based MHPs in addition to various other generic surface defects in all MHPs. Panels reproduced with permission from: **f**, ref. [83], AAAS; **i**, ref. [89], Springer Nature Limited. Panel **c** reproduced with permission from ref. [11], Springer Nature Limited.

also create a less-constrained environment for the α-to-δ transition to occur and propagate (Fig. 7a). Furthermore, the octahedral tilt in the $FAPbI_3$ lattice was found to influence the phase transition[50]. It is tailorable by controlling the IGD density and functionalizing GBs and surfaces, which distorts the lattice internally or externally. Yun et al.[23] used AFM to capture the onset of moisture-induced degradation in an $FAPbI_3$ film and confirmed the prominent role of GBs in trapping moisture and triggering a polymorphic transition, although it remains unclear how the transition front moves across bulk $FAPbI_3$ grains. These mechanisms understandings were leveraged to invent state-of-the-art fabrication methods for $FAPbI_3$ PSCs, in which rationally selected chemical molecules are used to passivate the GBs and surfaces (Fig. 7b). Jeong et al.[11] showed that, by incorporating $HCOO^-$ pseudohalide anions into the precursor solution that sequentially interact with $FAPbI_3$ grain and GBs in the solid film, PSCs with a certified 25.2% PCE and superior device operational stability were achieved (Fig. 7c), attesting the role of GBs and surfaces in the phase transition dominated degradation process.

Mixed-halide MHPs, widely studied for wide-bandgap top cells in tandem, undergo light-induced halide segregation, which converts

single-phase MHPs into separated I-rich and Br-rich phases and thus lowers the V_{OC} (ref. [71]). This degradation mode is dominated by ion movement (Fig. 7d). Therefore, a striking phase segregation will occur where the diffusivity of I and Br differ to the largest extent. Evidence to now points to GB as the microstructure type that influence this process mostly. Tang et al.[26] monitored time-dependent PL evolutions separately at the GB and grain-interior regions. The grain interior was found to retain its intrinsic bandgap emission, whereas redshifted PL is gradually generated at the GB region, indicative of the formation of an I-rich domain. Facile halide segregation at the GBs may also be related to relaxed strain structures[82]. Therefore, to reduce the GB structural dimensionality is an effective mitigation method (Fig. 7e). Kim et al.[83] used a PEA(I_xSCN_{1-x}) additive to form 2D second-phases at the GBs of wide-bandgap MHPs (inset of Fig. 7f). An optimal formation of 2D phases at the GBs is achieved by tuning the additive composition, which results in a much more stable PSC performance than those of control devices without GB tailoring or with unoptimized GB tailoring (Fig. 7f).

For Sn–Pb and Pb-free Sn MHPs, the low oxidation resistance of Sn(II) is a major hurdle, which is subject to its interaction with environmental O_2 species[84]. As illustrated in Fig. 7g, one possible scenario for the degradation mode follows two steps: (1) O_2 adsorption by MHP surfaces and (2) O_2 penetration via GBs that feature a high degree of disorder in their pristine states. Park et al.[85] showed that the O_2 adsorption energy of pristine $FAPb_{0.5}Sn_{0.5}I_3$ is as low as −1.01 eV, which favours O_2–MHP interaction. Metallic doping can be helpful to increase the O_2 adsorption energy for surfaces and improve the GB disorder, thus enhancing MHP stability. This is consistent with the proposed scenario. Nevertheless, it is challenging to study the atomic-level mechanisms of oxygen-induced degradation of Sn MHPs, because it starts on surfaces that are highly disordered and the relative disordered structure of surfaces limits the studies using local structure characterization methods, such as solid-state NMR spectroscopy[86]. With regard to devices, multifunctional additives have been used to passivate MHP surfaces (Fig. 7h) and address both Sn oxidation and all the general processing and stability issues for MHPs[25,87,88]. Lin et al.[87] demonstrated a zwitterionic antioxidant as a suitable additive that interacts with both Sn and halide vacancies of the surface and GBs of mixed Sn–Pb MHP thin films. Zwitterions are also known as a surfactant that facilitates the solution formation of compact grain microstructures. IGDs, such as Sn vacancies, may also be modulated as their formation can be affected by synthetic conditions. As a result, a stable and efficient perovskite–perovskite tandem device is achieved. Later, Lin et al.[89] further studied the absorption stability of passivators on Sn–Pb MHP surfaces, which guided the discovery of the 4-trifluoromethylphenylammonium cation passivator that leads to a 26.4% certified PCE perovskite–perovskite tandem with over 600 hours of 90% retention of the initial PCE (T90) operational stability (Fig. 7i).

Conclusion and outlook

Past research that entailed the use of various characterization techniques led to significant evidence to support the outstanding role of the three MHP microstructure types (GBs, IGDs and surfaces) in photophysical properties and chemical stability. Meanwhile, the dynamic, coupled interactions of MHP microstructures with photocarriers, intrinsic ions and extrinsic species and/or stimuli offers a fascinating playground for further exploration. Furthermore, the (opto)mechanical properties of PSCs have started to draw attention as interfacial and bulk mechanical degradations can considerably impact the long-term stability in addition to the (photo)chemical processes[18]. The interplay of cracking with various MHP morphological defects emerges as a new frontier of stability studies in PSCs. All these fundamental energy sciences will be translated for perovskite photovoltaic engineering to create efficient and durable tandems and multijunctions and large-area modules with even more complex MHP microstructures and morphological defects. We briefly propose the following research directions to set solid foundations for PSC development.

The first is to probe hidden microstructures and their underdetermined effects. As mentioned earlier, the relative ease of identifying surface-probed GBs matured their fundamental understanding quickly, and has guided the field to achieve high-performance PSCs from single junctions to tandems that embrace various MHP compositions. However, the microstructural details of many essential morphological defects remain hidden, for example, the buried GBs near film bottom surfaces, IGD characteristics of different types in state-of-the-art MHPs and the novel device heterointerfaces with a high coherence and long-range ordering established in the record-performance PSCs[58,59,65,90–92]. In fact, such omissions in considering all these hidden and/or buried features could be one of the causes for the existing discrepancies in the GB roles in PSCs. Therefore, probing hidden microstructures is likely to lead to corrected understandings on established findings. Future studies urgently call for innovations in materials sample preparation methods and experimental design to unlock the characterization of these hidden microstructures.

The second is to enable in situ correlated characterizations and theory-guided interpenetration. Correlated and in situ microscopic studies will be the next key step to decisively understand microstructure–property–performance relationships in PSCs, as the complex nature of the MHP system introduces tangling factors that are difficult to investigate separately in conventional systematic, macroscopic studies. The development of combinatorial and correlated experimental instrumentation suites is needed to visualize the effect of microstructures on the motion of photocarriers, ions and/or molecules and cracks in the MHPs under controlled conditions. Especially, the recent advances in X-ray and electron microscopies have even demonstrated their excellent capability of the in situ (operando) characterization of full (opto)electronic devices, leverageable to probe the structural and functional dynamics in PSCs in real time. In addition, multiscale theoretical simulations may be further developed to model and statistically capture the observed microstructures. Given the large data sets produced from in situ correlated characterizations, machine-learning algorithms will rapidly emerge to interpret the results and guide a more targeted exploration.

The third is to harness microstructural imperfections for better PSCs. Earlier, we mainly indicated the detrimental roles of many known microstructural imperfections in MHPs. Counterintuitively, there could be an interesting space to harness the potential merits of these imperfections. Taking the example of electronic benign CTBs, it would be intriguing to see whether we can utilize this to tailor strain in MHPs to enhance their chemical stability. Also, microstructural imperfections may be leveraged for (opto)mechanical merits. For example, intragrain dislocations in MHPs may be controlled to build tougher interfaces in PSCs. Again, all these will link back to the microscopic structure–property–performance relationship, which attests to the significance of this fundamental investigation.

Received: 8 June 2021; Accepted: 13 July 2022;
Published online: 19 September 2022

References

1. Kojima, A., Teshima, K., Shirai, Y. & Miyasaka, T. Organometal halide perovskites as visible-light sensitizers for photovoltaic cells. *J. Am. Chem. Soc.* **131**, 6050–6051 (2009).
The first report on the use of MHPs for solar cell applications.
2. Kim, H.-S. et al. Lead iodide perovskite sensitized all-solid-state submicron thin film mesoscopic solar cell with efficiency exceeding 9%. *Sci. Rep.* **2**, 591 (2012).

3. Heo, J. H. et al. Efficient inorganic–organic hybrid heterojunction solar cells containing perovskite compound and polymeric hole conductors. *Nat. Photon.* **7**, 486–491 (2013).
4. Burschka, J. et al. Sequential deposition as a route to high-performance perovskite-sensitized solar cells. *Nature* **499**, 316–319 (2013).
5. Jeon, N. J. et al. Solvent engineering for high-performance inorganic–organic hybrid perovskite solar cells. *Nat. Mater.* **13**, 897–903 (2014).
6. Jeon, N. J. et al. Compositional engineering of perovskite materials for high-performance solar cells. *Nature* **517**, 476–480 (2015).
7. Yang, W. S. et al. High-performance photovoltaic perovskite layers fabricated through intramolecular exchange. *Science* **348**, 1234–1237 (2015).
8. Yang, W. S. et al. Iodide management in formamidinium-lead-halide-based perovskite layers for efficient solar cells. *Science* **356**, 1376–1379 (2017).
9. Jung, E. H. et al. Efficient, stable and scalable perovskite solar cells using poly (3-hexylthiophene). *Nature* **567**, 511–515 (2019).
10. Jiang, Q. et al. Surface passivation of perovskite film for efficient solar cells. *Nat. Photon.* **13**, 460–466 (2019).
11. Jeong, J. et al. Pseudo-halide anion engineering for α-$FAPbI_3$ perovskite solar cells. *Nature* **592**, 381–385 (2021).
12. Liu, M., Johnston, M. B. & Snaith, H. J. Efficient planar heterojunction perovskite solar cells by vapour deposition. *Nature* **501**, 395–398 (2013).
The first report on the use of MHPs in a thin-film solar-cell-device configuration.
13. Min, H. et al. Perovskite solar cells with atomically coherent interlayers on SnO_2 electrodes. *Nature* **598**, 444–450 (2021).
14. Green, M. A., Ho-Baillie, A. & Snaith, H. J. The emergence of perovskite solar cells. *Nat. Photon.* **8**, 506–514 (2014).
15. Zhou, Y., Zhou, H., Deng, J., Cha, W. & Cai, Z. Decisive structural and functional characterization of halide perovskites with synchrotron. *Matter* **2**, 360–377 (2020).
16. Zhou, Y., Game, O. S., Pang, S. & Padture, N. P. Microstructures of organometal trihalide perovskites for solar cells: their evolution from solutions and characterization. *J. Phys. Chem. Lett.* **6**, 4827–4839 (2015).
17. Dunlap-Shohl, W. A., Zhou, Y., Padture, N. P. & Mitzi, D. B. Synthetic approaches for halide perovskite thin films. *Chem. Rev.* **119**, 3193–3295 (2018).
18. Dai, Z. et al. Interfacial toughening with self-assembled monolayers enhances perovskite solar cell reliability. *Science* **372**, 618–622 (2021).
19. Rothmann, M. U. et al. Atomic-scale microstructure of metal halide perovskite. *Science* **370**, eabb5940 (2020).
The first atomic-scale observation of MHP thin-film microstructures using scanning TEM.
20. Kim, M. C. et al. Advanced characterization techniques for overcoming challenges of perovskite solar cell materials. *Adv. Energy Mater.* **11**, 2001753 (2021).
21. Rothmann, M. U., Li, W., Etheridge, J. & Cheng, Y. B. Microstructural characterisations of perovskite solar cells–from grains to interfaces: techniquells, features, and challenges. *Adv. Energy Mater.* **7**, 1700912 (2017).
22. Li, W. et al. Subgrain special boundaries in halide perovskite thin films restrict carrier diffusion. *ACS Energy Lett.* **3**, 2669–2670 (2018).
23. Yun, J. S. et al. Humidity-induced degradation via grain boundaries of $HC(NH_2)_2PbI_3$ planar perovskite solar cells. *Adv. Funct. Mater.* **28**, 1705363 (2018).
24. Zong, Y. et al. Continuous grain-boundary functionalization for high-efficiency perovskite solar cells with exceptional stability. *Chem* **4**, 1404–1415 (2018).
25. Zong, Y., Zhou, Z., Chen, M., Padture, N. P. & Zhou, Y. Lewis-adduct mediated grain-boundary functionalization for efficient ideal-bandgap perovskite solar cells with superior stability. *Adv. Energy Mater.* **8**, 1800997 (2018).
26. Tang, X. et al. Local observation of phase segregation in mixed-halide perovskite. *Nano Lett.* **18**, 2172–2178 (2018).
27. Jiang, J. et al. Carrier lifetime enhancement in halide perovskite via remote epitaxy. *Nat. Commun.* **10**, 4145 (2019).
28. Xiao, X. et al. Benign ferroelastic twin boundaries in halide perovskites for charge carrier transport and recombination. *Nat. Commun.* **11**, 2215 (2020).
29. Meggiolaro, D., Mosconi, E. & De Angelis, F. Formation of surface defects dominates ion migration in lead-halide perovskites. *ACS Energy Lett.* **4**, 779–785 (2019).
30. Stecker, C. et al. Surface defect dynamics in organic–inorganic hybrid perovskites: from mechanism to interfacial properties. *ACS Nano* **13**, 12127–12136 (2019).
31. Li, F. et al. Regulating surface termination for efficient inverted perovskite solar cells with greater than 23% efficiency. *J. Am. Chem. Soc.* **142**, 20134–20142 (2020).
32. Zheng, G. et al. Manipulation of facet orientation in hybrid perovskite polycrystalline films by cation cascade. *Nat. Commun.* **9**, 2793 (2018).
33. Leblebici, S. Y. et al. Facet-dependent photovoltaic efficiency variations in single grains of hybrid halide perovskite. *Nat. Energy* **1**, 16093 (2016).
An early study on the heterogeneous photovoltaic response on the surface of MHP thin films.
34. Khanna, R. & Sahajwalla, V. in *Treatise on Process Metallurgy* (ed. Seetharaman, S.) 287–393 (Elsevier, 2014).
35. Tennyson, E. M., Doherty, T. A. S. & Stranks, S. D. Heterogeneity at multiple length scales in halide perovskite semiconductors. *Nat. Rev. Mater.* **4**, 573–587 (2019).
36. Banerjee, S. & Saha, H. Grain boundary effects in polycrystalline silicon solar cells. *Solar Cells* **28**, 77–94 (1990).
37. Tritscher, P. & Broadbridge, P. Grain boundary grooving by surface diffusion: an analytic nonlinear model for a symmetric groove. *Proc. R. Soc. Lond. A* **450**, 569–587 (1995).
38. Zhou, Y., Sternlicht, H. & Padture, N. P. Transmission electron microscopy of halide perovskite materials and devices. *Joule* **3**, 641–661 (2019).
39. Cai, S. et al. Atomically resolved electrically active intragrain interfaces in perovskite semiconductors. *J. Am. Chem. Soc.* **144**, 1910–1920 (2022).
The first study to image the atomic-scale microstructure of IGDs in PSCs.
40. Song, J., Zhou, Y., Padture, N. P. & Huey, B. D. Anomalous 3D nanoscale photoconduction in hybrid perovskite semiconductors revealed by tomographic atomic force microscopy. *Nat. Commun.* **11**, 3308 (2020).
The first 3D imaging of grain boundary networks in MHP thin films.
41. Ercius, P., Alaidi, O., Rames, M. J. & Ren, G. Electron tomography: a three-dimensional analytic tool for hard and soft materials research. *Adv. Mater.* **27**, 5638–5663 (2015).
42. Shao, Y. et al. Grain boundary dominated ion migration in polycrystalline organic–inorganic halide perovskite films. *Energy Environ. Sci.* **9**, 1752–1759 (2016).
43. Jariwala, S. et al. Local crystal misorientation influences non-radiative recombination in halide perovskites. *Joule* **3**, 3048–3060 (2019).
44. Rothmann, M. U. et al. Direct observation of intrinsic twin domains in tetragonal $CH_3NH_3PbI_3$. *Nat. Commun.* **8**, 14547 (2017).
The first microscopic observation of twin domains in MHP thin films.
45. Thind, A. S. et al. Atomic structure and electrical activity of grain boundaries and Ruddlesden–Popper faults in cesium lead bromide perovskite. *Adv. Mater.* **31**, 1805047 (2019).
46. Cheng, S. Y., Ho, N. J. & Lu, H. Y. Transformation-induced twinning: the 90° and 180° ferroelectric domains in tetragonal barium titanate. *J. Am. Chem. Soc.* **89**, 2177–2187 (2006).
47. Li, W. et al. The critical role of composition-dependent intragrain planar defects in the performance of $MA_{1-x}FA_xPbI_3$ perovskite solar cells. *Nat. Energy* **6**, 624–632 (2021).
The first systematic study on the relationship between IGD characteristics and MHP properties and performance.
48. Reiche, M. et al. On the electronic properties of a single dislocation. *J. Appl. Phys.* **115**, 194303 (2014).
49. Xue, J., Wang, R. & Yang, Y. The surface of halide perovskites from nano to bulk. *Nat. Rev. Mater.* **5**, 809–827 (2020).
50. Doherty, T. A. S. et al. Stabilized tilted-octahedra halide perovskites inhibit local formation of performance-limiting phases. *Science* **374**, 1598–1605 (2021).
51. Li, N., Niu, X., Chen, Q. & Zhou, H. Towards commercialization: the operational stability of perovskite solar cells. *Chem. Soc. Rev.* **49**, 8235–8286 (2020).
52. Kong, J. et al. CO_2 doping of organic interlayers for perovskite solar cells. *Nature* **594**, 51–56 (2021).
53. Kubicki, D. J., Stranks, S. D., Grey, C. P. & Emsley, L. NMR spectroscopy probes microstructure, dynamics and doping of metal halide perovskites. *Nat. Rev. Chem.* **5**, 624–645 (2021).
54. Dahlman, C. J., Kubicki, D. J. & Reddy, G. N. M. Interfaces in metal halide perovskites probed by solid-state NMR spectroscopy. *J. Mater. Chem. A* **9**, 19206–19244 (2021).
55. Chen, Y. et al. Surface termination of $CsPbBr_3$ perovskite quantum dots determined by solid-state NMR spectroscopy. *J. Am. Chem. Soc.* **142**, 6117–6127 (2020).
56. Yuan, J., Bao, H., Liu, H., Wang, S. & Li, X. Mixed solvent atmosphere induces the surface termination state transition of perovskite to achieve matched energy level alignment. *Chem. Eng. J.* **424**, 130508 (2021).
57. Liu, Y. et al. Atomistic origins of surface defects in $CH_3NH_3PbBr_3$ perovskite and their electronic structures. *ACS Nano* **11**, 2060–2065 (2017).
58. Azmi, R. et al. Damp heat-stable perovskite solar cells with tailored-dimensionality 2D/3D heterojunctions. *Science* **376**, 73–77 (2022).
59. Chen, H. et al. Quantum-size-tuned heterostructures enable efficient and stable inverted perovskite solar cells. *Nat. Photon.* **16**, 352–358 (2022).
60. de Quilettes, D. W. et al. Impact of microstructure on local carrier lifetime in perovskite solar cells. *Science* **348**, 683–686 (2015).
The first microstructure–property correlated study revealing the detrimental effects of GBs in MHPs.
61. Li, W. et al. Direct characterization of carrier diffusion in halide–perovskite thin films using transient photoluminescence imaging. *ACS Photon.* **6**, 2375–2380 (2019).
62. Yun, J. S. et al. Benefit of grain boundaries in organic–inorganic halide planar perovskite solar cells. *J. Phys. Chem. Lett.* **6**, 875–880 (2015).

63. Chu, Z. et al. Impact of grain boundaries on efficiency and stability of organic–inorganic trihalide perovskites. *Nat. Commun.* **8**, 2230 (2017).
64. Pham, H. T., Duong, T., Weber, K. J. & Wong-Leung, J. Insights into twinning formation in cubic and tetragonal multi-cation mixed-halide perovskite. *ACS Mater. Lett.* **2**, 415–424 (2020).
65. Tan, S. et al. Stability-limiting heterointerfaces of perovskite photovoltaics. *Nature* **605**, 268–273 (2022).
The first study that mechanistically revealed the negative impact of regular passivation strategies on the stability of heterointerfaces in PSCs.
66. Juarez-Perez, E. J. et al. Photodecomposition and thermal decomposition in methylammonium halide lead perovskites and inferred design principles to increase photovoltaic device stability. *J. Mater. Chem. A* **6**, 9604–9612 (2018).
67. Wang, Q. et al. Scaling behavior of moisture-induced grain degradation in polycrystalline hybrid perovskite thin films. *Energy Environ. Sci.* **10**, 516–522 (2017).
68. Alberti, A. et al. Pb clustering and PbI_2 nanofragmentation during methylammonium lead iodide perovskite degradation. *Nat. Commun.* **10**, 2196 (2019).
69. Ju, M.-G. et al. Toward eco-friendly and stable perovskite materials for photovoltaics. *Joule* **2**, 1231–1241 (2018).
70. Eperon, G. E. et al. Formamidinium lead trihalide: a broadly tunable perovskite for efficient planar heterojunction solar cells. *Energy Environ. Sci.* **7**, 982–988 (2014).
71. Knight, A. J. & Herz, L. M. Preventing phase segregation in mixed-halide perovskites: a perspective. *Energy Environ. Sci.* **13**, 2024–2046 (2020).
72. Awais, M., Kirsch, R. L., Yeddu, V. & Saidaminov, M. I. Tin halide perovskites going forward: frost diagrams offer hints. *ACS Mater. Lett.* **3**, 299–307 (2021).
73. Hu, M. et al. Sub-1.4-eV bandgap inorganic perovskite solar cells with long-term stability. *Nat. Commun.* **11**, 151 (2020).
74. Jena, A. K., Kulkarni, A. & Miyasaka, T. Halide perovskite photovoltaics: background, status, and future prospects. *Chem. Rev.* **119**, 3036–3103 (2019).
75. Wang, R. et al. Prospects for metal halide perovskite-based tandem solar cells. *Nat. Photon.* **15**, 411–425 (2021).
76. Cao, J. & Yan, F. Recent progress in tin-based perovskite solar cells. *Energy Environ. Sci.* **14**, 1286–1325 (2021).
77. Zhang, F. et al. Advances in two-dimensional organic–inorganic hybrid perovskites. *Energy Environ. Sci.* **13**, 1154–1186 (2020).
78. Li, H. & Zhang, W. Perovskite tandem solar cells: from fundamentals to commercial deployment. *Chem. Rev.* **120**, 9835–9950 (2020).
79. Zhou, Y., Poli, I., Meggiolaro, D., De Angelis, F. & Petrozza, A. Defect activity in metal halide perovskites with wide and narrow bandgap. *Nat. Rev. Mater.* **6**, 986–1002 (2021).
80. Zhou, Y., Yang, M., Pang, S., Zhu, K. & Padture, N. P. Exceptional morphology-preserving evolution of formamidinium lead triiodide perovskite thin films via organic-cation displacement. *J. Am. Chem. Soc.* **138**, 5535–5538 (2016).
81. Wang, Z. et al. Additive-modulated evolution of $HC(NH_2)_2PbI_3$ black polymorph for mesoscopic perovskite solar cells. *Chem. Mater.* **27**, 7149–7155 (2015).
82. Chen, Z., Brocks, G., Tao, S. & Bobbert, P. A. Unified theory for light-induced halide segregation in mixed halide perovskites. *Nat. Commun.* **12**, 2687 (2021).
83. Kim, D. et al. Efficient, stable silicon tandem cells enabled by anion-engineered wide-bandgap perovskites. *Science* **368**, 155–160 (2020).
84. Jiang, X. et al. Tin halide perovskite solar cells: an emerging thin-film photovoltaic technology. *Acc. Mater. Res.* **2**, 210–219 (2021).
85. Park, C., Choi, J., Min, J. & Cho, K. Suppression of oxidative degradation of tin–lead hybrid organometal halide perovskite solar cells by Ag doping. *ACS Energy Lett.* **5**, 3285–3294 (2020).
86. Kubicki, D. J. et al. Local structure and dynamics in methylammonium, formamidinium, and cesium tin(II) mixed-halide perovskites from ^{119}Sn solid-state NMR. *J. Am. Chem. Soc.* **142**, 7813–7826 (2020).
87. Lin, R. et al. Monolithic all-perovskite tandem solar cells with 24.8% efficiency exploiting comproportionation to suppress Sn(II) oxidation in precursor ink. *Nat. Energy* **4**, 864–873 (2019).
88. Liu, X. et al. Efficient and stable tin perovskite solar cells enabled by amorphous-polycrystalline structure. *Nat. Commun.* **11**, 2678 (2020).
89. Lin, R. et al. All-perovskite tandem solar cells with improved grain surface passivation. *Nature* **603**, 73–78 (2022).
90. Kim, M. et al. Conformal quantum dot–SnO_2 layers as electron transporters for efficient perovskite solar cells. *Science* **375**, 302–306 (2022).
91. Li, X. et al. Constructing heterojunctions by surface sulfidation for efficient inverted perovskite solar cells. *Science* **375**, 434–437 (2022).
92. Dong, Q. et al. Interpenetrating interfaces for efficient perovskite solar cells with high operational stability and mechanical robustness. *Nat. Commun.* **12**, 973 (2021).

Acknowledgements

Y.Z. acknowledges the start-up grants, the Interdisciplinary Matching Scheme, Initiation Grant—Faculty Niche Research Areas (IG-FNRA) 2020/21 of HKBU, and the Early Career Scheme (no. 22300221) from the Hong Kong Research Grant Council. L.M.H. acknowledges funding from the Engineering and Physical Sciences Research Council (EPSRC) UK, and support from TUM-IAS through a Hans Fischer Senior Fellowship. A.K.-Y.J. thanks the support from the Lee Shau Kee Chair Professorship and the Innovation and Technology Fund (ITS/497/18FP, GHP/021/18SZ). M.S. acknowledges the German Research Foundation (DFG, GRK 2642, SPP 2196).

Competing interests

The authors declare no competing interests.

Additional information

Correspondence should be addressed to Yuanyuan Zhou.

Peer review information *Nature Energy* thanks Dominik Kubicki and the other, anonymous, reviewer(s) for their contribution to the peer review of this work.